WAVES IN RANDOM AND COMPLEX MEDIA, 2017
https://doi.org/10.1080/17455030.2017.1392647

Taylor & Francis
Taylor & Francis Group

Low-grazing angle propagation and scattering by an object above a highly-conducting rough sea surface in a ducting environment from an accelerated MoM

C. Bourlier

IETR (Institut d'Electronique et de Télécommunications de Rennes) Laboratory, LUNAM Université, Université de Nantes, Polytech Nantes, Nantes Cedex 3, France

ABSTRACT

In a previous paper, by combining three techniques, i.e. Subdomain Decomposition Iterative Method (SDIM), Adaptive Cross Approximation (ACA), and Forward–Backward Spectral Acceleration (FBSA), from the Method of Moments (MoM), a high-efficiency calculation of the propagation and scattering in ducting maritime environments has been proposed. In this paper, this algorithm is updated by adding a perfectly conducting object above the sea surface, assumed to be highly conducting, which makes the environment very complex. Then, to quantify the effect of the object on the total scattered field, the coherent and incoherent powers, with and without object, are simulated by considering a surface of 800,000 unknowns (length of 6 km and a frequency of 5 GHz).

ARTICLE HISTORY
Received 24 January 2017
Accepted 28 September 2017

AQ1

1. Introduction

In coastal and maritime regions, the microwave propagation is affected by the high variability of the meteorological parameters in space and time. This variability leads to respective changes in the tropospheric refractive index n. The ducting is present for a small percent of time but it significantly influences the radar and communication systems working in the microwave range. Then, the presence of a duct strongly affects the propagation, but also jointly, the scattering from the sea surface. The addition of an object in the duct makes the problem to solve very complex due to the possible multiple interactions between the object and the sea surface.

For a longtime, The Parabolic Wave Equation (PWE) method combined with SSF (Split-Step Fourier) has been widely used to model radiowave propagation in a cone centered on the paraxial direction over highly conducting irregular surfaces in an inhomogeneous atmosphere. For a complete review of this method, see the textbook of Levy [1] and the references therein. The great advantage of the PWE-SSF method is that it can deal with most real-life inhomogeneous environments and is that it fast (based on the calculation of successions of FFTs). Its main drawback is the underlying paraxial approximation leading to an approximation of the propagator (that is, the Green's function) and the boundary conditions are determined from a heuristic way, for instance from the Ament reflection

CONTACT C. Bourlier christophe.bourlier@univ-nantes.fr

coefficient [2–6]. In addition, the conventional PWE is a one-way model, which implies that it handles only the forward propagating waves and neglects the backward propagating waves. That is why, two-way PWE and FE (Finite Element) schemes have been published [7–9].

The well-known Method of Moments (MoM) [10–12] is a way of solving rigorously the scattering problem by converting the Boundary Integral Equation (BIE) into a linear system, in which the impedance matrix must be inverted to determine the surface currents. Then, the scattered field is computed by radiating the surface currents. For a ducting environment, the main drawback of the MoM is that the Green's function (propagator) is known only for a small class of refractive index profiles [13,14]. That is why, when the BIE method is applied [15–20], the propagator is usually derived under the PWE approximation. The duct effect is significant over a long distance, which means that the size (related to the surface length) of the linear system to solve is huge for practical applications. Combining three techniques, i.e. Subdomain Decomposition Iterative Method (SDIM) [21], Adaptive Cross Approximation (ACA) [22,23], and Forward–Backward Spectral acceleration (FBSA) [24], from the Method of Moments (MoM), Bourlier [20] published a high-efficiency calculation method of the propagation and scattering in ducting maritime environments. The resulting method is named 'SDIM+FBSA+ACA'.

The SDIM allows us to split up the surface into sub-surfaces, the ACA allows us to accelerate the coupling steps between the sub-surfaces and FBSA allows us to accelerate the calculation of the local interactions on the sea sub-surfaces. It is important to underline that the FBSA algorithm can be applied if the sub-medium above the sub-surface is assumed to be homogeneous (no ducting effect). For a closed surface, like an object above a sea surface, the FB (and also, the FBSA) does not converge. Then, for only the sub-surface associated to the object, a direct LU decomposition is applied instead of the FBSA technique. It is the purpose of this paper. In addition, to quantify the effect of the object on the total scattered field, the coherent and incoherent powers, with and without object, are computed. To my knowledge, it is the first time that such a problem is solved rigorously by a numerical method, based on the MoM.

This paper is organized as follows. Section 2 briefly summarizes the SDIM combined with ACA and FBSA by giving the resulting complexity. Section 3 presents numerical results and the last section gives concluding remarks.

2. Mathematical formulation

In this section, the SDIM+FBSA+ACA method is briefly summarized, updated to include the object and, extended to two levels in order to solve huge problems.

2.1. SDIM+FBSA+ACA method

The MoM [10] for the electromagnetic scattering problem results in a set of linear system of algebraic equations that are cast in matrix form as $\bar{\boldsymbol{Z}}\boldsymbol{X} = \boldsymbol{b}$, where $\bar{\boldsymbol{Z}}$ is the known MoM impedance matrix of sizes $N \times N$, $\boldsymbol{b}$ is an $N \times 1$ known excitation vector, and $\boldsymbol{X}$, is the unknown solution vector of sizes $N \times 1$, with N the number of unknowns needed to accurately describe the current distribution on the surface.

Since the sea surface is highly conductive for microwave frequencies, the impedance (or Leontovich) boundary condition (IBC) is applied to calculate the impedance matrix obtained by discretizing the integral equations from the MoM [10–12,20]. Then, the elements of the impedance matrix depend on the Green function g (propagator). To obtain a closed-form expression of g, the PWE approximation combined with a near-field correction (in near field, the Green function is exact) is applied. In [20], g is derived for a parabolic profile defined as $n(z) = 1 - \epsilon_1 z + \epsilon_2 z^2/2$, where z is the height. The advantage of using such a profile, instead of a linear canonical profile ($\epsilon_2 = 0$), is that the gradient of the refractive index can change with z and then, the rays associated to the scattered field can leave the duct or can be trapped in the duct. This phenomenon is met for practical applications.

For a very long sea surface, N becomes prohibitively large, and this rules out the option of a direct matrix inversion for computing the vector $\boldsymbol{X}$. To overcome this issue, the Subdomain Decomposition Iterative Method (SDIM) is developed. SDIM consists in splitting the sea surface Σ into K sub-surfaces Σ_i ($\Sigma = \Sigma_1 \cup \Sigma_2 \cup \ldots \cup \Sigma_K$). Then, it first computes the surface current on each isolated sub-surface Σ_k ($\boldsymbol{X}_k$) and next, from an iterative scheme, it updates the current density by interacting the sub-domains between them. Then

$$\boldsymbol{X} \approx \sum_{p=0}^{P=P_{\text{SDIM}}} \boldsymbol{Y}^{(p)}, \tag{1}$$

where

$$\begin{cases} \boldsymbol{Y}_k^{(0)} = \bar{\boldsymbol{Z}}_{k,k}^{-1} \boldsymbol{v}_k \\ \boldsymbol{Y}_k^{(p)} = -\bar{\boldsymbol{Z}}_{k,k}^{-1} \displaystyle\sum_{n=1, n\neq k}^{K} \bar{\boldsymbol{Z}}_{n,k} \boldsymbol{Y}_n^{(p-1)} \quad p > 0 \end{cases}, \tag{2}$$

and $\boldsymbol{Y}_k^{(p)}$ is the surface current at the order p on the sub-surface k, $\boldsymbol{v}_k$ ($\boldsymbol{v}_k = \boldsymbol{b}_k$ for $p = 0$) the incident field on the sub-surface k and $\bar{\boldsymbol{Z}}_{n,k}$ the impedance matrix between the sub-surfaces n and k (propagation of the scattered field from n toward k). The order of convergence P_{SDIM} is obtained from the criterion on RRE (Relative Residual Error) defined by

$$\text{RRE} = \frac{\|\boldsymbol{X}^{(p)} - \boldsymbol{X}^{(p-1)}\|}{\|\boldsymbol{X}^{(p)}\|}. \tag{3}$$

Typically, the threshold of SDIM is chosen as $\epsilon_{\text{SDIM}} = 0.01$.

In Equation (2), to speed up the calculation of the matrix–vector product $\bar{\boldsymbol{Z}}_{n,k} \boldsymbol{Y}_n^{(p-1)}$, and to reduce the memory requirement to store the coupling matrices $\{\bar{\boldsymbol{Z}}_{n,k}\}$ between the sub-surfaces, the Adaptive Cross Approximation (ACA) is applied, which is a compression technique. For more details, see references [20–23]. In addition, to accelerate the calculation of the local interactions on each sub-surface (in Equation (2), term $\bar{\boldsymbol{Z}}_{k,k}^{-1} \boldsymbol{v}_k$), the Forward–Backward Spectral Acceleration (FBSA) method is applied. It is important to underline that FBSA can be applied if the sub-medium is homogeneous. A detailed explanation of FBSA can be found in [12,20,24]. The resulting method, named 'SDIM+FBSA+ACA', is presented in details in [21].

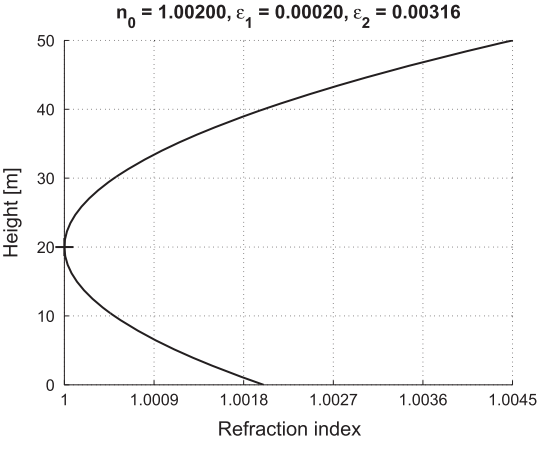

Figure 1. Height vs. the refractive index.

The resulting complexity and the memory requirement of SDIM+FBSA+ACA are then, respectively

$$C_{\text{SDIM}}^{\text{ACA+FBSA}} = N\Big[\mathcal{O}(M_{\text{FBSA}})\left(1+P_{\text{SDIM}}\right) + P_{\text{SDIM}}M\left(K-1\right)\left(1-\bar{\tau}_{\text{ACA}}\right)\Big], \tag{4}$$

and

$$M_{\text{SDIM}}^{\text{ACA+FBSA}} = N\left[\mathcal{O}(M_{\text{FBSA}}) + M\left(K-1\right)\left(1-\bar{\tau}_{\text{ACA}}\right)\right], \tag{5}$$

where

- N is the number of unknowns on the sea surface.
- K the number of sub-surfaces (or sub-blocks). Typically, it ranges from 5 to 10.
- $M = N/K$ the number of unknowns on each sub-surface assumed to be the same for all the sub-surfaces.
- M_{FBSA} is related to the number of elements of the strong interactions n_{FBSA}. Typically, $M_{\text{FBSA}} \ll M$ and n_{FBSA} equals the integer part of $0.154 \times 0.6u_{10}^2/\Delta x \approx 0.10u_{10}^2/\Delta x$, where u_{10} is the wind speed defined at 10 meters above the sea mean level and Δx, the surface sampling step.
- P_{SDIM} the order of convergence of SDIM. Typically, it ranges from 4 to 8.
- $\bar{\tau}_{\text{ACA}}$ the mean compression ratio of ACA. Typically it ranges from 0.98 (small problems) to 0.9999 (huge problems). Then, in the above equations, $1-\bar{\tau}_{\text{ACA}}$ tends toward zero as M increases.

In conclusion, $C_{\text{SDIM}}^{\text{ACA+FBSA}}$ and $M_{\text{SDIM}}^{\text{ACA+FBSA}}$ are nearly proportional to N in terms of complexity and memory requirement, instead of $\mathcal{O}(N^3)$ and N^2, respectively, if a direct LU decomposition is applied on the matrix $\bar{\boldsymbol{Z}}$. These fundamental properties will allow us to solve huge propagation and scattering problems.

A means to reduce the number of iterations of SDIM, P_{SDIM}, is to overlap the adjacent sub-surfaces of few tens of samples (n_{OL}), to decrease the contribution of the edge diffraction coming from the finiteness of the sub-surfaces.

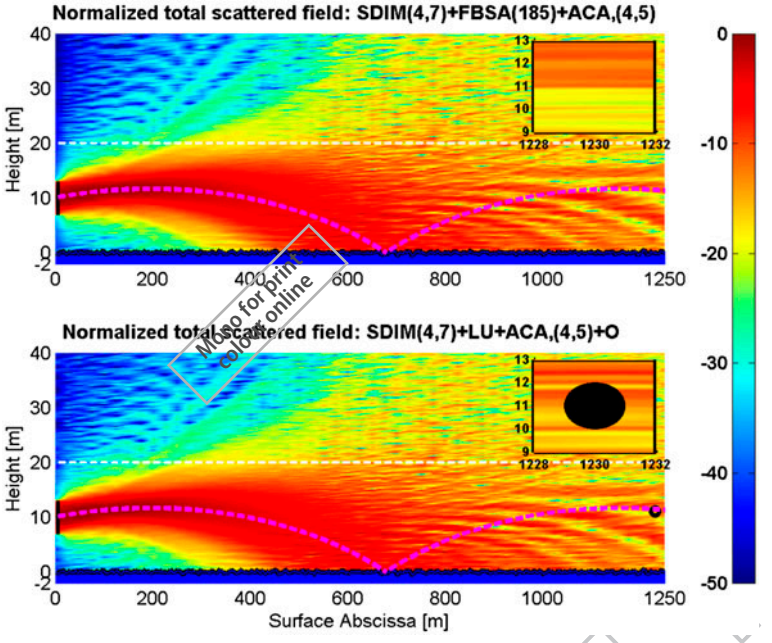

Figure 2. Modulus of the normalized total field and on the grid (x_0, z_0) with $x_0 \in [0; L = 1250]$ m and $z_0 \in [0; 40]$ m. Top: without object. Bottom: with object.

2.2. Introduction of the object

For a closed object, the FB (also the FBSA) does not converge. Then the SDIM+FBSA+ACA algorithm is modified to solve this issue. Indeed, for each sub-surface, any method (either rigorous or asymptotic) can be applied to calculate the local interactions (surface currents). For the sub-block associated to the object, a direct LU decomposition is applied to solve the linear system instead of the FBSA. Since, the size of this sub-block is much smaller than those of the other sub-blocks (associated to the sub-surfaces), the complexity and memory requirement of the resulting method are nearly affected. Then, to include the object, the algorithm is generalized to any sizes of the sub-blocks.

2.3. Extension to two levels

Articles [20,21] showed that if the number of blocks K is too large (typically larger than 10), the SDIM can fail. It is the first condition. On the other hand, to apply the FBSA, the sub-domains must be homogeneous, which means that the number of samples M ($M = N/K$) per block must not be too large, or in other words, K must be large enough. This second condition is in contradiction with the first one. Then, in [20], the SDIM+FBSA+ACA has been extended to level 2 to satisfy these two conditions in order to simulate huge problems. To satisfy condition 1, the sub-surface lengths of level 1 are large enough, whereas to satisfy condition 2, the sub-surface lengths of level 2 (each sub-surface of level 1 is split up into K_2 sub-surfaces of level 2) are small enough to apply the FBSA. The rule to determine K_2 is given in section IV-C of [20].

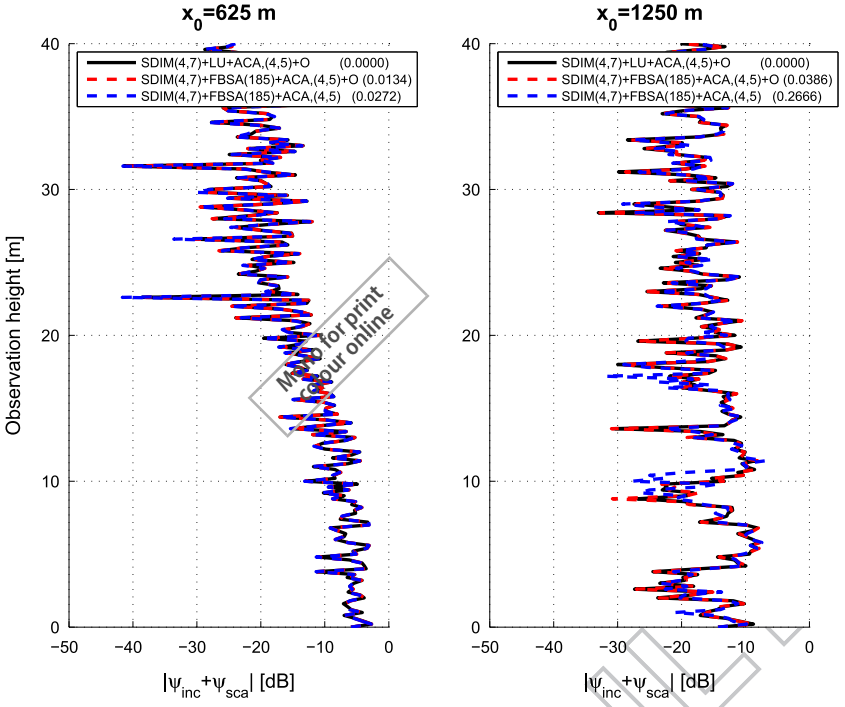

Figure 3. Modulus of the normalized total field vs. the height z_0 and for given $x_0 = \{625, 1250\}$ m.

In Equation (2), level 2 means that the SDIM+FBSA+ACA is applied again for the calculation of the vector–matrix product $\bar{\boldsymbol{Z}}_{k,k}^{-1}\boldsymbol{v}_k$.

3. Numerical results

For the simulations, it is assumed that the rough sea surface height is a stationary Gaussian stochastic process with zero mean value, and that the height spectrum obeys the Elfouhaily et al. hydrodynamic spectrum [25], in which the key parameter is the wind speed u_{10} at 10 meters above the sea surface.

3.1. Incident field and scattered field

The incident field (vector $\boldsymbol{v}$ in Equation (2) for $p = 0$) is defined as the field produced by the source (antenna) that would exist in the duct in the absence of the rough surface. When the BIE approach is used to simulate the problem of propagation over a rough surface in a ducting medium, it is appropriate to calculate the field produced by the source, the initial field, $\psi_{\text{inc}}^{a}(z_a)$, on a given vertical plane defined at $x = 0$. The incident field on the rough surface, $\psi_{\text{inc}}(\boldsymbol{r})$ ($\boldsymbol{r} \in \Sigma$), is then evaluated by propagating the initial field from the vertical plane onto the rough surface using the ducting medium propagator.

For grazing angles ($\theta_{\text{inc}} \to \pi/2$), Bourlier et al. showed that this field can be approximated as [19] (Equation (C5))

$$\psi_{\text{inc}}^{a}(z_a) \approx \exp\left(jk_0\left(z_a - z_{a,0}\right)\cos\theta_{\text{inc}} - \frac{\left(z_a - z_{a,0}\right)^2}{g_z^2}\right), \tag{6}$$

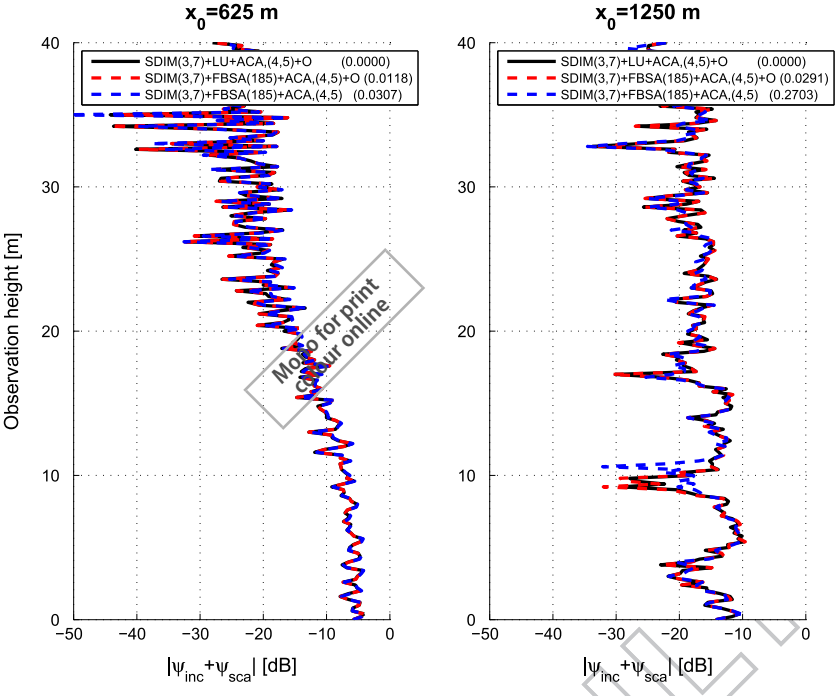

Figure 4. Same variations as in Figure 3 but for the TM polarization.

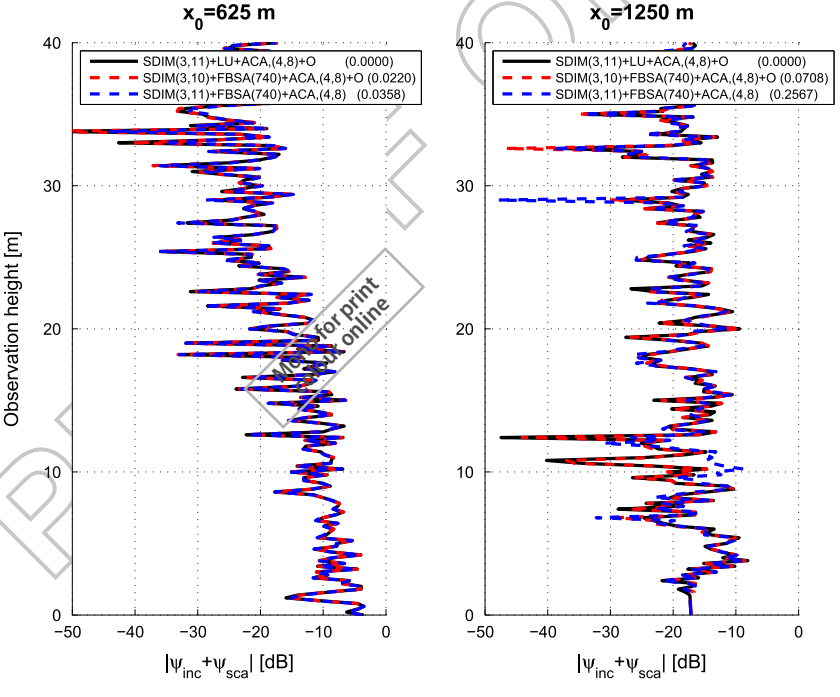

Figure 5. Same variations as in Figure 3 but the wind speed is $u_{10} = 10$ m/s.

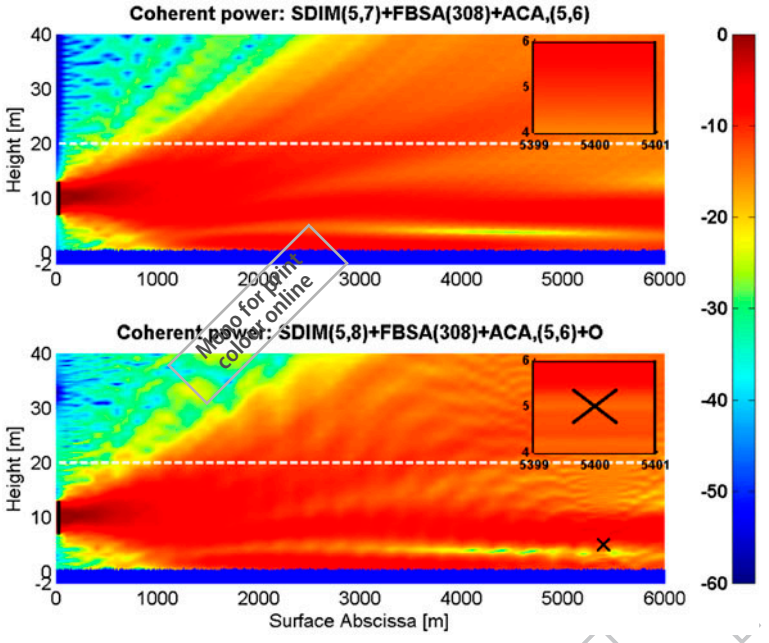

Figure 6. Normalized coherent power and on the grid (x_0, z_0) with $x_0 \in [0; L = 6000]$ m and $z_0 \in [0; 40]$ m. Top: without object. Bottom: with object. TE polarization and $u_{10} = 5$ m/s.

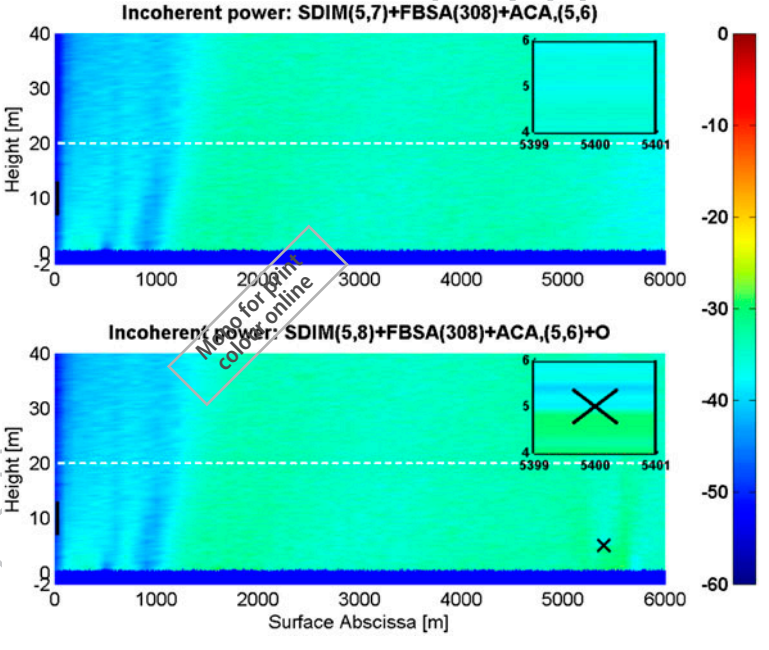

Figure 7. Normalized incoherent power and on the grid (x_0, z_0) with $x_0 \in [0; L = 6000]$ m and $z_0 \in [0; 40]$ m. Top: without object. Bottom: with object. TE polarization and $u_{10} = 5$ m/s.

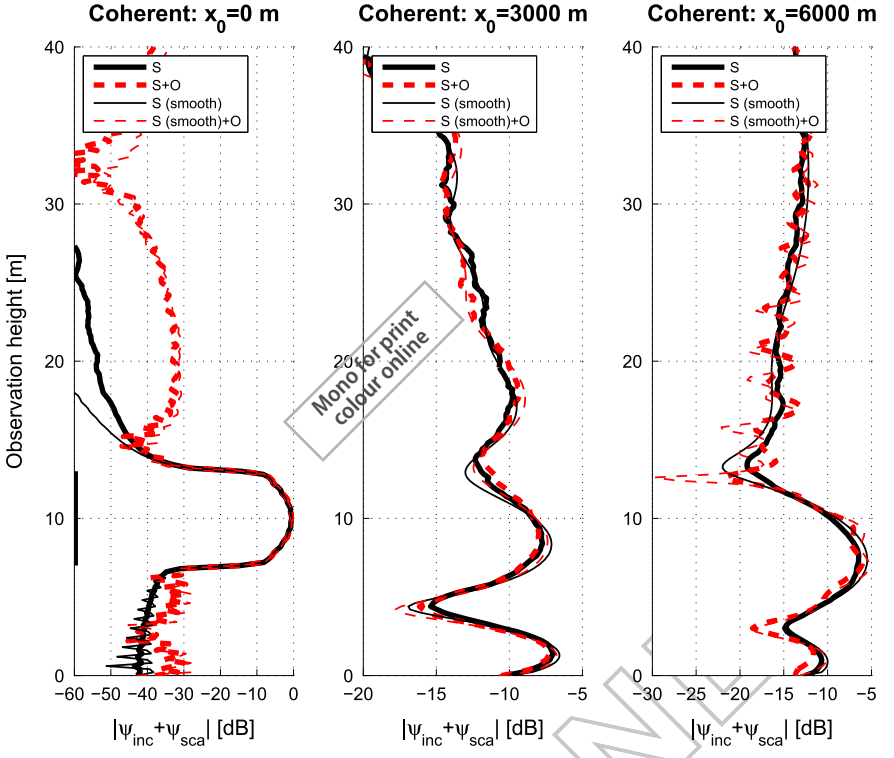

Figure 8. Normalized coherent power vs. the height z_0 and for given $x_0 = \{0, 3000, 6000\}$ m. TE polarization and $u_{10} = 5$ m/s.

where

- θ_{inc} is the look angle measured from the positive z-axis;
- $\psi^a_{\text{inc}}(z_a)$ the incident field on the surface S_a (z_a varies);
- $z_{a,0}$ the center of the antenna (constant number) with respect to z (the abscissa of the antenna is set to zero);
- g_z the vertical footprint (in the plane $x = 0$).

Introducing $\boldsymbol{b}_a$, the vector of components $\psi^a_{\text{inc}}(z_a)$ discretized on the surface S_a, Bourlier [20] showed that the incident field on the surface can be expressed as a matrix–vector product as $\boldsymbol{b} = -2jk_0 \bar{\boldsymbol{Z}}^{\boldsymbol{r}_a \to \boldsymbol{r}}_{TE} \boldsymbol{b}_a$, where $\bar{\boldsymbol{Z}}_{TE}$ is the impedance matrix obtained from the Dirichlet boundary condition. In addition, it is shown that the scattered field, $\boldsymbol{b}_{\text{sca}}$, can be also expressed as a matrix–vector product as $\boldsymbol{b}_{\text{sca}} = -\bar{\boldsymbol{Z}}^{\boldsymbol{r} \to \boldsymbol{r}'}_{TE,TM} \boldsymbol{X}$, where $\bar{\boldsymbol{Z}}^{\boldsymbol{r} \to \boldsymbol{r}'}_{TE,TM}$ is the impedance matrix obtained from the IBC boundary condition and for the TE and TM polarizations, respectively. $\boldsymbol{r}$ stands for a point on the surface and $\boldsymbol{r}'$ denotes a point in the duct.

For a huge problem, the computations of the vectors $\boldsymbol{b}$ and $\boldsymbol{b}_{\text{sca}}$ are very time consuming. Thus, to overcome this issue, the ACA algorithm (per block) is also applied. Typically, the mean compression ratios to calculate $\boldsymbol{b}$ and $\boldsymbol{b}_{\text{sca}}$ are 0.98 and 0.90, respectively.

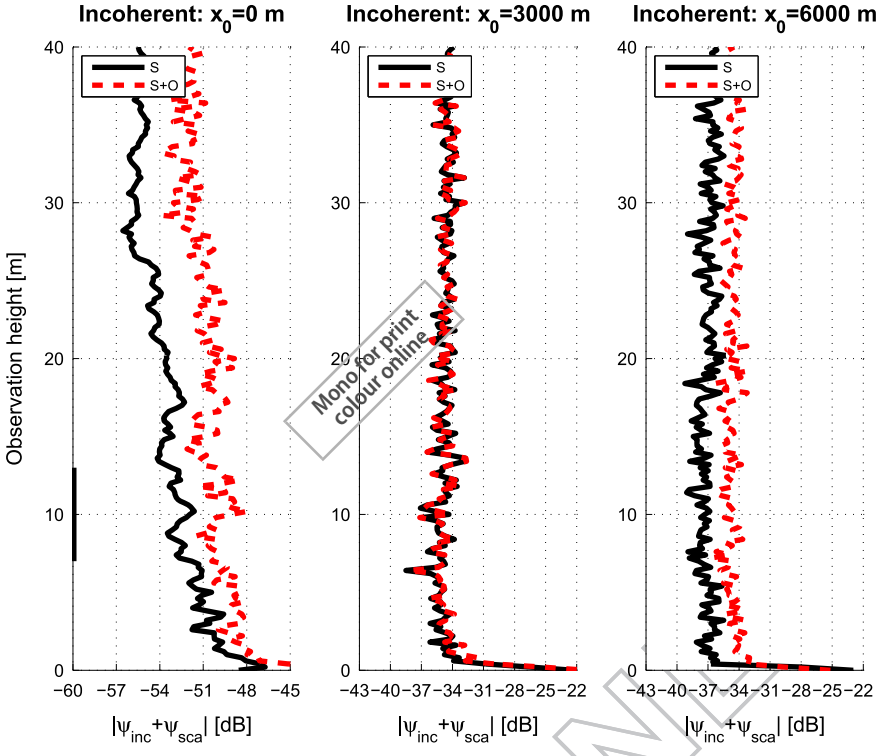

Figure 9. Normalized incoherent power vs. the height z_0 and for given $x_0 = \{0, 3000, 6000\}$ m. TE polarization and $u_{10} = 5$ m/s.

3.2. *Validation of the updated method*

The simulation parameters are reported in the first column of Table 1. The subscripts '1' and '2' refer to the variables defined at levels 1 and 2, respectively.

The parabolic profile of the refractive index, $n(z)$, is plotted in Figure 1 vs. the height z. As we can see for $z \in [0; z_c = \epsilon_1/\epsilon_2^2]$ ($n'(z_c) = 0$), the gradient of $n(z)$ is negative whereas for $z > z_c$, it is positive. The use of a parabolic profile allows us to consider jointly a positive and a negative gradient, which is not possible from a linear profile.

For all figures, the total field will be normalized by the maximum of the modulus of the incident field.

Figure 2 plots the modulus of the normalized total field and on the grid (x_0, z_0) with $x_0 \in [0; L]$ and $z_0 \in [0; 40]$ m. At $x = 0$, the thick vertical line shows the extension of the source (antenna). The horizontal dashed curve plots the height $z_c = 20$ m and the dashed curve plots the ray trajectory (for a flat sea surface) calculated for an initial point of coordinates $(0, z_{a,0})$ and of initial slope $\cot\theta_{\text{inc}}$. It is expressed in Appendix C of [20].

In the title of each sub-plot, the labels mean:

- SDIM($P_{1,\text{SDIM}}$,$\bar{P}_{2,\text{SDIM}}$)+FBSA(n_{FBSA})+ACA, (K_1, K_2) (without object),
- SDIM($P_{1,\text{SDIM}}$,$\bar{P}_{2,\text{SDIM}}$)+FBSA(n_{FBSA})+ACA, (K_1, K_2) + O (with object),

where $\bar{P}_{2,\text{SDIM}}$ is the mean convergence order of SDIM at level 2.

The object is a circular cylinder of coordinates (x_c, z_c) and of radius a_c given in Table 1.

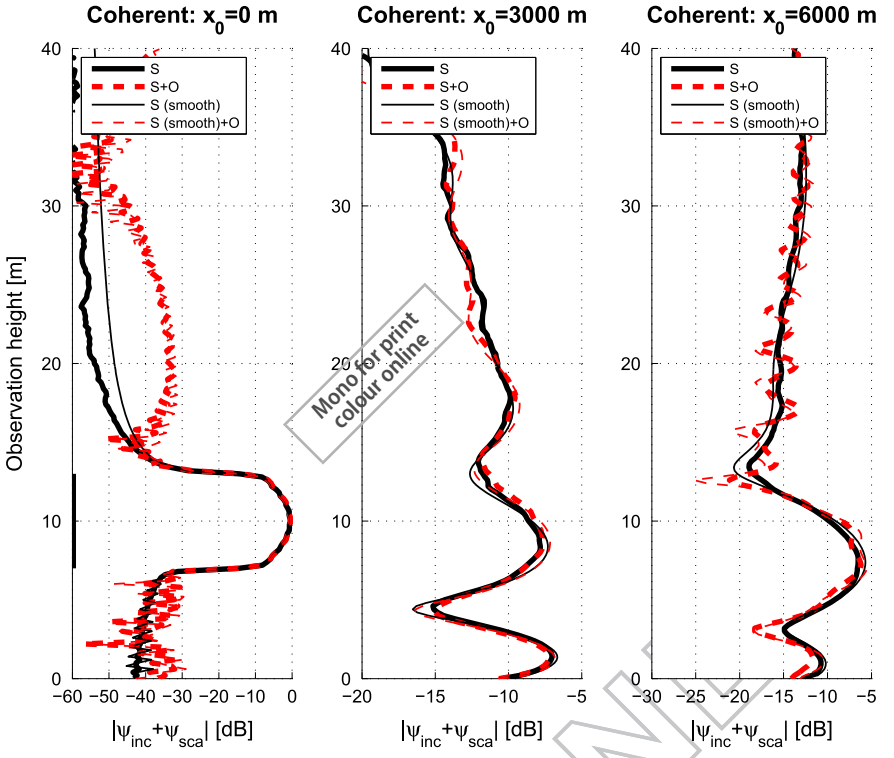

Figure 10. Same variations as in Figure 8, but for the TM polarization ($u_{10} = 5$ m/s).

Before the first bounce defined at the abscissa $x = X_2 \approx 678$ m (appendix C of [20]), the main contribution is given by the incident field. The incident field is trapped in the duct (defined for $z \in [0; z_c]$) because the height of the antenna does not exceed the critical height $z_{a,c} = z_c - \cot\theta_{\text{inc}}/\epsilon_2$ (appendix C of [20]), for which the ray leaves the duct. Indeed, $z_{a,c} = 14.47$ m $>$ max $(z_a) = 13$ m.

Unlike the incident field, a part of the scattered field radiated by the surface currents produced by the first bounce is not trapped and can leave the duct. Due to the surface roughness, the angles of the first bounces $\theta_{r,1}$ are defined around $\bar{\theta}_{r,1} \approx 86.47^{\text{o}}$ (case of a flat surface defined from appendix C of [20]). If $\theta_{r,1} < \text{arccot}(\epsilon_2 z_c) = 86.38^{\text{o}}$ ($z_{a,c} = 0$), then the corresponding ray leaves the duct, which explains the behavior of the total field in the region $z_0 > z_c$. In addition, for this region, the ray trajectories are convex because the gradient of the refractive index is positive. For a linear refractive index profile, this effect cannot occur because the gradient is always negative for any height.

With object, the ACA compression ratio at level 1 $\tau_{\text{ACA},1} \in [0.997; 0.999]$ with a mean value of 0.998, whereas the mean compression at level 2 $\tau_{\text{ACA},2} \in [0.986; 0.993]$ with a mean value of 0.988. Without object, the ACA compression ratio at level 1 $\tau_{\text{ACA},1} \in [0.997; 0.999]$ with a mean value of 0.998, whereas the mean compression at level 2 $\tau_{\text{ACA},2} \in [0.984; 0.994]$ with a mean value of 0.988. Then, the presence of the object decreases slightly $\tau_{\text{ACA},2}$ and the SDIM convergence orders $\{P_{1,\text{SDIM}}, \bar{P}_{2,\text{SDIM}}\}$ do not change with object. In general $\bar{\tau}_{\text{ACA},1} > \bar{\tau}_{\text{ACA},2}$, because $\bar{\tau}_{\text{ACA}}$ increases as the size of the matrix to compress increases. Then, ACA is very efficient for a huge problem.

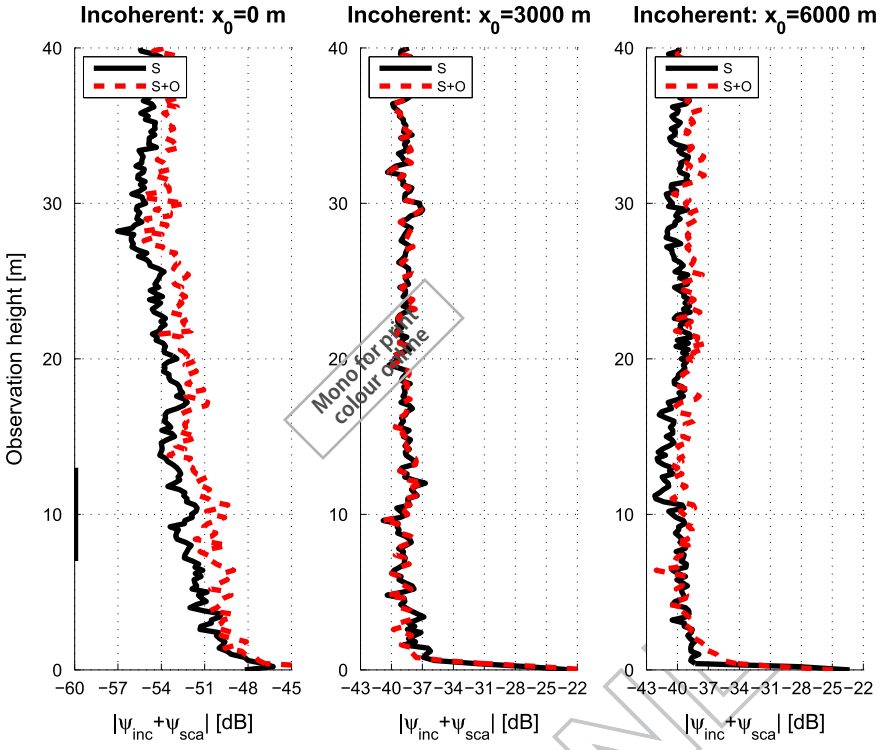

Figure 11. Same variations as in Figure 9, but for the TM polarization ($u_{10} = 5$ m/s).

Table 1. Simulation parameters. The duct parameters ϵ_1 and ϵ_2 are obtained from n_0 and n_c as $\epsilon_1 = 2(n_0 - n_c)/z_c$ and $\epsilon_2 = \sqrt{2(n_0 - n_c)}/z_c$. The height z_c is defined as $n'(z_c) = 0$. The surface sampling step is $\Delta x = \lambda_0/8$. The second column is for Figures 2–5. The third column is for Figures 6–9.

Duct parameter $n(0) = n_0$	1.002	1.00003
Duct parameter $n(z_c) = n_c$	1	1
Duct parameter z_c [m]	20	20
Wavelength λ_0 [m]	0.1	0.06
Incidence angle θ_{inc} [°]	89	89.9
Polarization	TE	TE
Vertical footprint g_z [m]	3	3
Transmitter center $z_{a,0}$ [m]	10	10
Transmitter heights z_a [m]	$z_a \in [7; 13]$	$z_a \in [7; 13]$
Sea permittivity ϵ_{r3}	$70.4 + 40.6j$	$69.2 + 35.7j$
Surface length L [m]	1250	6000
Wind speed u_{10} [m/s]	5	5
Number of unknowns N	100,000	800,000
Numbers of blocks (K_1, K_2)	(4,5)	(5,6)
Threshold of ACA ϵ_{ACA}	0.001	0.001
Threshold of FB ϵ_{FB}	0.01	0.01
Thresholds of SDIM $(\epsilon_{1,\text{SDIM}}, \epsilon_{2,\text{SDIM}})$	(0.05,0.01)	(0.05,0.01)
Overlapping $(n_{1,\text{OL}}, n_{2,\text{OL}})$	(20,20)	(20,20)
Cylinder: (x_c, z_c, a_c) [m]	(1230,11,1)	(-,-,-)
Cross: (x_c, z_c, l_c) [m]	(-,-,-)	(5400,5,1)

To better see the difference in Figures 2, 3 plots the modulus of the normalized total field vs. the height z_0 and for the given abscissa $x_0 = \{625, 1250\}$ m. In the legend, the number

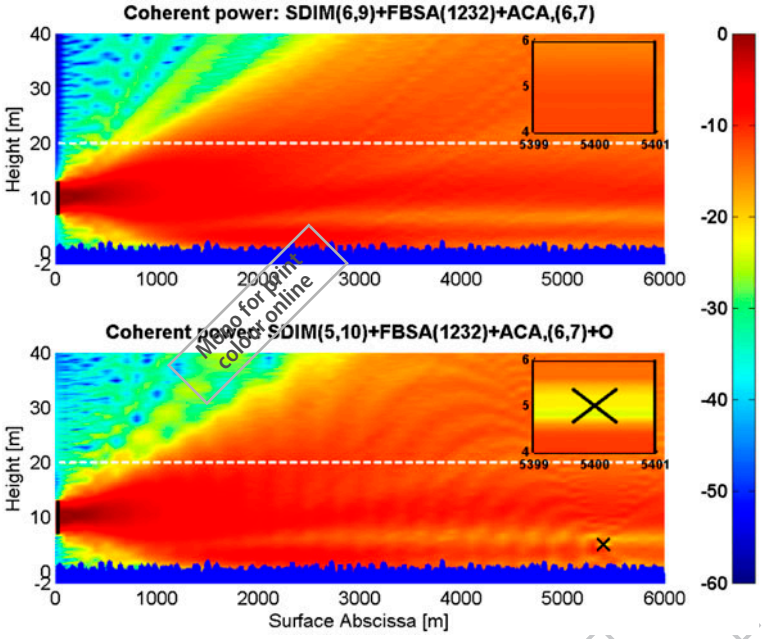

Figure 12. Same variations as in Figure 6 but for $u_{10} = 10$ m/s.

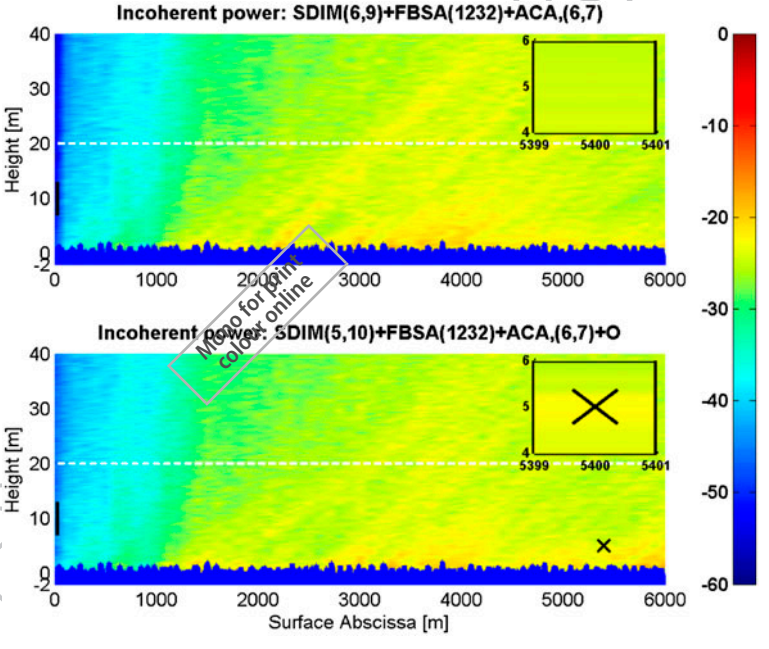

Figure 13. Same variations as in Figure 7 but for $u_{10} = 10$ m/s.

within parenthesis gives the value of the RRE (Equation (3)) defined for the total field and computed for each x_0.

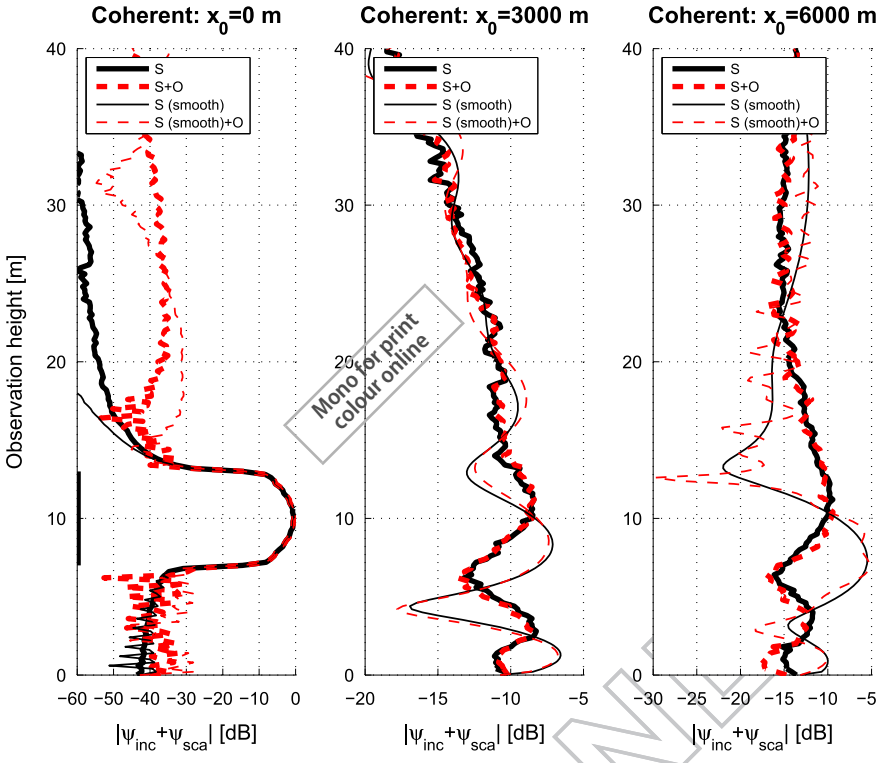

Figure 14. Same variations as in Figure 8 but for $u_{10} = 10$ m/s.

As we can see, SDIM+LU+ACA (a direct LU inversion is applied instead of FBSA) and SDIM+FBSA+ACA results match well, which shows that the numbers of blocks $\{K_1, K_2\}$ are enough. Indeed, the choices of K_1 and K_2 are governed by the fact that the lengths of the sub-surfaces of level 2 are small enough to use the Green function in free space to compute the local interactions on each sub-surface from FBSA. In addition, as x_0 increases, the RRE slightly increases because the refraction effect increases with x_0. Comparing the results with and without object, Figure 3 shows that for $x_0 = 625$ m, the object has a small impact on the total scattered field, whereas for $x_0 = 1250$ m, differences occur in the duct region ($z \in [0; 20]$ m).

Figure 4 plots the same variations as in Figure 3, but for the TM polarization. In comparison to TE polarization, $P_{1,\mathrm{SDIM}}$ is smaller (from 4 to 3), because the SDIM converges faster for the TM polarization.

Figure 5 plots the same variations as in Figure 3, but the wind speed is $u_{10} = 10$ m/s (the numbers of blocks $(K_1, K_2) = (4, 8)$ also change). As the wind speed increases, the SDIM convergence orders $\{P_{1,\mathrm{SDIM}}, \bar{P}_{2,\mathrm{SDIM}}\}$ increase because the interactions between the far blocks are stronger.

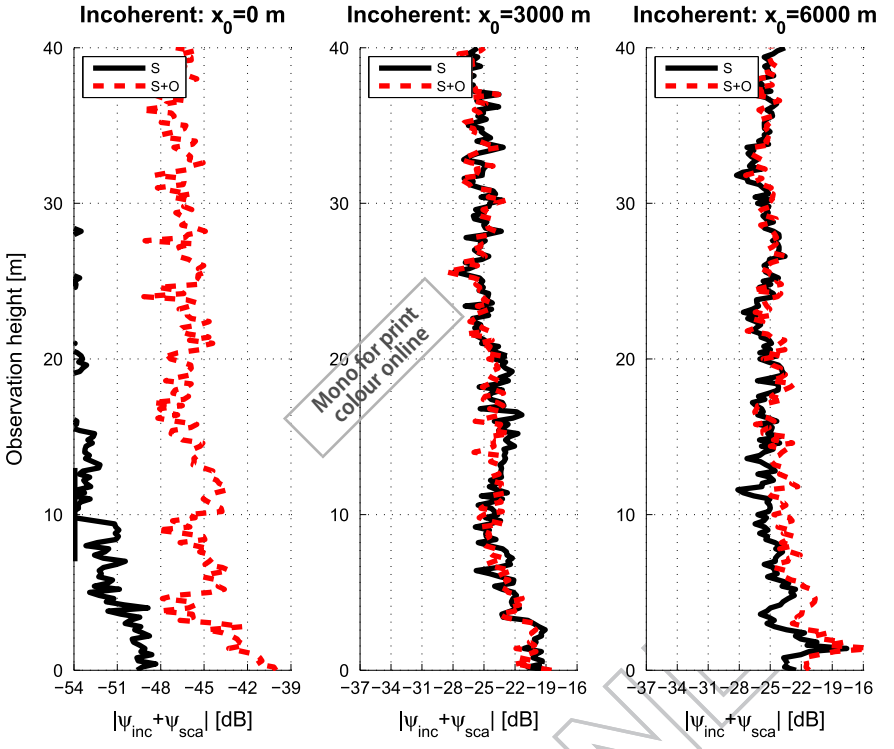

Figure 15. Same variations as in Figure 9 but for $u_{10} = 10$ m/s.

3.3. *Coherent and incoherent powers*

Several independent sea surfaces are generated as realizations of the Gaussian random process using the spectral method. The average coherent and incoherent powers are then computed. The simulation parameters are reported in third column of Table 1. The object is a cross (to produce the dihedral effect) of length 1 meter and inclined of an angle of $\pi/4$. The number of realizations is 40, enough to reach the convergence.

Figure 6 plots the normalized coherent power on the grid (x_0, z_0) with $x_0 \in [0; L = 6000]$ m and $z_0 \in [0; 40]$ m. Top: without object. Bottom: with object. Figure 7 plots the same variations, but for the normalized *incoherent* scattered power.

As we can see, the levels of the incoherent component are much smaller than the coherent ones because the sea surface electromagnetic roughness is small and the incident field does not contribute. It is related to the Rayleigh parameter, defined as $R_a = k_0 \sigma_z \cos\theta_{\text{inc},1} \approx 0.13$, where $k_0 = 2\pi/\lambda_0 \approx 104.7$ rad/m (wave number), $\sigma_z \approx 0.162$ m (the surface height standard deviation) for $u_{10} = 5$ m/s and, $\theta_{\text{inc},1} \approx 89.57^{\text{o}}$ (the incidence angle of the first bounce on the surface). For the region around the object, the incoherent component decreases slightly.

To better see the differences, Figures 8 and 9 plot the normalized coherent and incoherent powers vs. the height z_0 and for given $x_0 = \{0, 3000, 6000\}$ m. Figure 8 also plots the results obtained for a smooth sea surface and for $x = 0$ m, the vertical thin line indicates the antenna location (backscattering directions).

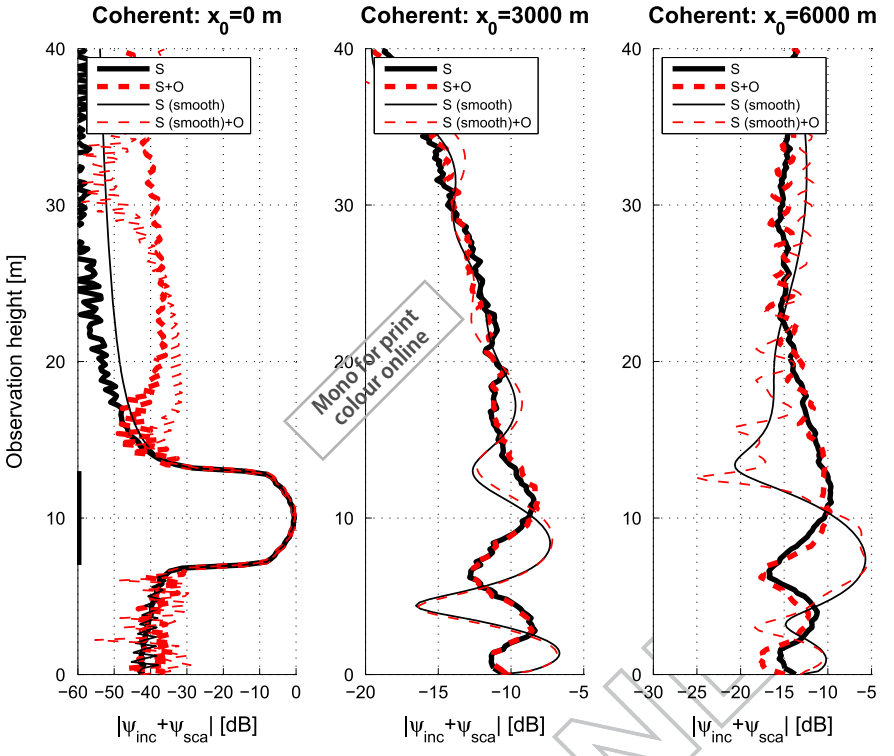

Figure 16. Same variations as in Figure 14 but for the TM polarization.

Figure 8 shows that the roughness modifies slightly the levels and a correlation (the extrema coincide) occurs with the results obtained for a smooth surface. This justifies the use of a modified reflection coefficient [3–6] (as the Ament model and similar models, in which the shadow is included) to account for the surface roughness. The difference between the results, with and without object, increases as x increases or for observation points closer to the object. In the backscattering directions, the difference is insignificant, whereas around $z = 20$ m, the object can be detected.

On the other hand, for the incoherent component, Figure 9 shows, for $x = 0$, that the object can be detected, but the level is small. In addition, near the surface, the incoherent component strongly decreases as z increases and, next, becomes nearly constant as z increases. This phenomenon has already been pointed out in [19] for a small problem.

Figures 10 and 11 plot the same variations as in Figures 8 and 9, but for the TM polarization. The results show similar results as in Figures 10 and 11, but the levels are slightly smaller. This comes from the fact that for the TM polarization, the Fresnel coefficient can be close to zero near the Brewster angle θ_B ($\mathcal{R}_{\mathrm{TE}}(\theta_B) \approx -0.014$ dB and $\mathcal{R}_{\mathrm{TM}}(\theta_B) \approx -1.120$ dB). For $\epsilon_r = 69.2 + 35.7j$, $\theta_B \approx 83.7^{\mathrm{o}}$, which is close to $\theta_{\mathrm{inc},1} \approx 89.57^{\mathrm{o}}$, the incidence angle of the first bounce on the surface. In comparison to the results obtained in [19] (small problems), this effect is less important for our configuration, because $\theta_{\mathrm{inc},1}$ is closer to 90 degrees (or farther than θ_B).

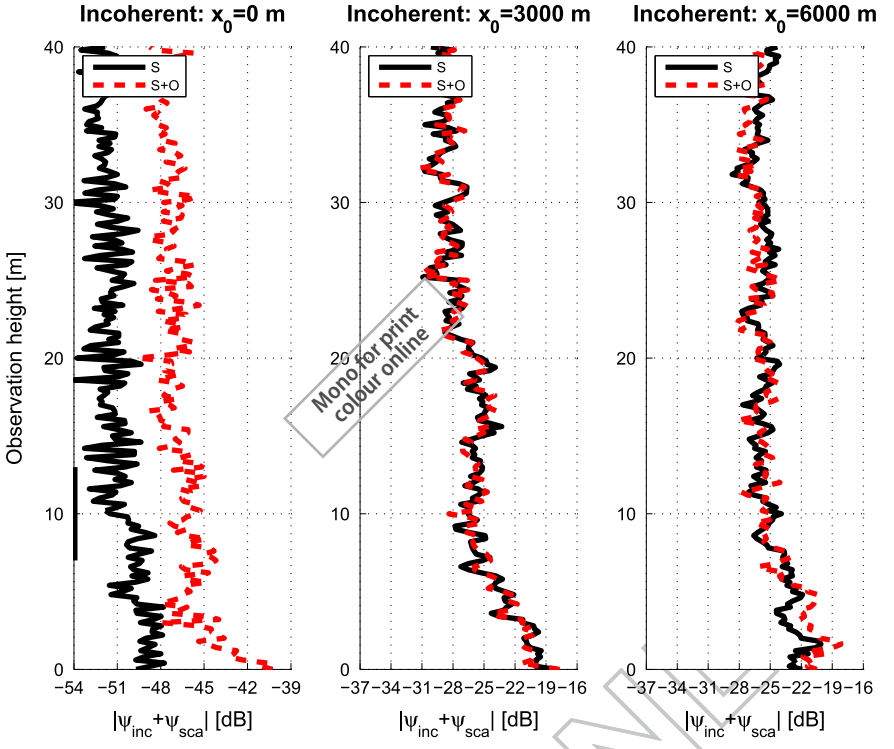

Figure 17. Same variations as in Figure 15 but for the TM polarization.

For one realization and for the TE polarization, the CPU times are of the order of 90 mn and 105 mn with and without object, respectively, whereas for the TM polarization, they are of the order of 50 mn and 60 mn, respectively. The memory requirement can be evaluated from Equation (5) as follows

$$M = K_1 K_2 N_{\text{FBSA}} + M_1 (K_1 - 1)\left(1 - \bar{\tau}_{\text{ACA},1}\right) + K_1 M_2 (K_2 - 1)\left(1 - \bar{\tau}_{\text{ACA},2}\right), \tag{7}$$

where

- N is the number of unknowns,
- K_1 is the number of blocks for the level 1,
- K_2 is the number of blocks for the level 2,
- $M_1 = N/K_1$ is the number of samples on the sub-surfaces of level 1,
- $M_2 = N/(K_1 K_2)$ is the number of samples on the sub-surfaces of level 2,
- N_{FBSA} is the number of elements of the strong integrations require for the FBSA. It is of the order of $4(N_2 + n_{\text{FBSA}}^2/2 + N_2 n_{\text{FBSA}})$.
- $\bar{\tau}_{\text{ACA},1}$ the mean compression ratio of all coupling matrices of level 1.
- $\bar{\tau}_{\text{ACA},2}$ the mean compression ratio of all coupling matrices of level 2.

Then, the memory requirement in Gbytes is obtained from the multiplication of M by $2 \times 8/(1024^3)$ (2 because it is a complex number and 8 for a double precision). The memory requirement is about 15 Gbytes ($n_{\text{FBSA}} = 308$) and numerically $M \approx K_1 K_2 N_{\text{FBSA}}$ since the

compression ratios are very close to 1. This shows that storage of all coupling matrices is minor.

Figures 12–15 plot the same variations as in Figures 6–9, respectively, but for $u_{10} = 10$ m/s.

Comparing Figures 13 with 7, as expected, the incoherent component increases because the surface is rougher. Since the surface height standard deviation σ_z is proportional to the square of u_{10}, the Rayleigh parameter R_a is multiplied by four. Figure 14 shows that the roughness modifies strongly the magnitude of the coherent component, and unlike Figure 8, the positions of the extrema are also strongly modified.

Figures 16 and 17 plot the same variations as in Figures 14 and 15, respectively, but for the TM polarization.

4. Conclusion

In this paper, the Boundary Integral Equation (BIE) Subdomain Decomposition Iterative method (SDIM), combined with ACA (Adaptive Cross Approximation) and FBSA (Forward–Backward Spectral-Acceleration), was employed to enhance the numerical efficiency of the SDIM for propagation and scattering from an object in a ducting environment and, above a finitely conducting rough sea surfaces. The combined SDIM/FBSA scheme substantially expedited the costly matrix–vector operation needed in the iterative FB procedure for calculating the surface currents on each sub-surface. In the same way, the ACA scheme substantially sped up the costly matrix–vector operation required for coupling steps between the sub-surfaces. In addition, for the sub-block associated to the object, a direct LU inversion is applied to calculate the local interactions. Since this block has a small size, the resulting complexity is slightly affected.

Numerical results obtained for wind speeds $u_{10} = \{5, 10\}$ m/s and for frequencies $f = \{3, 5\}$ GHz, showed that the convergence of SDIM increases slightly with object. In addition, in backscattering directions, the coherent component is not modified by the object, whereas the incoherent component increases in comparison to that calculated without object.

As a prospect of this paper, to enhance the numerical efficiency of SDIM, a parallelization can be done. Indeed, the pre-computations of impedance matrices $\bar{\boldsymbol{Z}}_{k,k}$ and $\bar{\boldsymbol{Z}}_{n,k}$ can be done in parallel and for a given order p of SDIM, the surface currents $\boldsymbol{Y}_k^{(p)}$ of each sub-surface k can be also computed in parallel.

Disclosure statement

AQ2 No potential conflict of interest was reported by the author.

References

[1] Levy M. Parabolic equation methods for electromagnetic wave propagation, Electromagnetic waves series. Vol. 45. London: The institution of Electrical Engineers; 2000.
[2] Ament WS. Toward a theory of reflection by a rough surfaces. Proc IRE. 1953;41:142–146.
[3] Fabbro V, Bourlier C, Combes PF. Forward propagation modeling above Gaussian rough surfaces by the parabolic wave equation: introduction of the shadowing effect. Prog Electromagnet Res. 2006;58:243–269.

[4] Freund DE, Woods NE, Ku H-C, et al. Forward radar propagation over a rough sea surface: a numerical assessment of the Miller-Brown approximation using a horizontally polarized 3-GHz line source. IEEE Trans Anten Propag. 2006;54(4):1192–1304.
[5] Freund DE, Woods NE, Ku H-C, et al. The effects of shadowing on modelling forward radar propagation over a rough sea surface. Waves Random Complex Media. 2008;18(3):387–408.
[6] Hristov TS, Anderson KD, Friehe CA. Scattering properties of the ocean surface: the Miller-Brown-Vegh model revisited. IEEE Trans Anten Propag. 2008;56(4):1103–1109.
[7] Ozgun O. Recursive two-way parabolic equation approach for modeling terrain effects in tropospheric propagation. IEEE Trans Anten Propag. 2009;57(9):2706–2714.
[8] Apaydin G, Ozgun O, Kuzuoglu M, et al. A novel two-way finite-element parabolic equation groundwave propagation tool: tests with canonical structures and calibration. IEEE Trans Geosci Remot Sensing. 2011;49(8):2887–2899.
[9] Wang K, Long Y. Propagation modeling over irregular terrain by the improved two-way parabolic equation method. IEEE Trans Anten Propag. 2012;60(9):4437–4471.
[10] Harrington RF. Field computation by moment method. New York (NY): Macmillan; 1968.
[11] Tsang L, Kong JA, Ding K-H, et al. Scattering of electromagnetics waves. Vol. II. Numerical simulations. Wiley series on remote sensing. New-York (NY); 2001.
[12] Bourlier C, Pinel N, Kubické G. Method of moments for 2D scattering problems Basic concepts and applications. Focus series in WAVES. London: Wiley-ISTE; 2013.
[13] Robins AJ. Exact solutions of the Helmholtz equation for plane wave propagation in a medium variable density and sound speed. J Acoust Soc Amer. 1993;93(3):1347–1352.
[14] Brekhovskikh LM. Waves in Layered media. 2nd ed. New York (NY): Academic Press; 1980.
[15] Uscinski BJ. Sound propagation with a linear sound-speed profile over a rough surface. J Acoust Soc Amer. 1993;94(1):491–498.
[16] Awadallah RS. Rough surface scattering and propagation over rough terrain in ducting environments [PhD dissertation]. Virginia Polytechnic Institute and State University. 1998.
[17] Awadallah RS, Brown GS. Low-grazing angle scattering from rough surfaces in a duct formed by a linear-square refractive index profile. IEEE Trans Anten Propag. 2000;48(5):1461–1474.
[18] Awadallah RS, Lamar MT, Kuttler JR. An accelerated boundary integral equation scheme for propagation over the ocean surface. Radio Science. 2002;37(5):1–15. DOI:10.1029/2001RS002536
[19] Bourlier C, Li H, Pinel N. Low-grazing angle propagation and scattering above the sea surface in the presence of a duct jointly solved by boundary integral equations. IEEE Trans Anten Propag. 2015;63(2):667–777.
[20] Bourlier C. Propagation and scattering in ducting maritime environments from an accelerated boundary integral equation. IEEE Trans Anten Propag. 2016;64(11):4794–4803.
[21] Bourlier C, Bellez S, Li H, et al. Sub-domain decomposition iterative method combined with ACA: an efficient technique for the scattering from a large highly conducting rough sea surface. IEEE Trans Anten Propag. 2015;63(2):659–666.
[22] Bebendorf M. Approximation of boundary element matrices. Numer Math. 2000;86(4):565–589.
[23] Zhao K, Vouvakis MN, Lee J-F. The adaptive cross approximation algorithm for accelerated method of moments computation of EMC problems. IEEE Trans Electromagnet Compat. 2005;47(4):763–773.
[24] Chou H-T, Johnson JT. A novel acceleration algorithm for the computation of scattering from rough surfaces with the Forward-Backward method. Radio Sci. 1998;33(5):1277–1287.
[25] Elfouhaily T, Chapron B, Katsaros K, et al. A unified directional spectrum for long and short wind-driven waves. J Geophys Res. 1997;102(C7):781–796.